Microbial anodes: What actually occurs inside pores?

Poehere Chong, Benjamin Erable, Alain Bergel

Microbial anodes: What actually occurs inside pores?

Poehere Chong [*], *Benjamin Erable*, *Alain Bergel*

Laboratoire de Génie Chimique, CNRS, Université de Toulouse, 4 Allée Emile Monso, 31432 Toulouse, France

ABSTRACT

Microbial anodes were formed under constant polarization either free in solution or inside channels of 1 mm or 5 mm height. Both the 5 mm and 1 mm high channels allowed the colonization of electrodes over several centimetres of penetration depth. The channel impacted the evolution of the biofilm along the electrode and limited the maximum current density to 5.4 $A.m^{-2}$, whatever the height, while 13.1 $A.m^{-2}$ was achieved with the free bioanodes. Several effects related to the channel configuration can be explained by a theoretical analysis of mass transfers. Nevertheless, other observations, such as the stabilizing effect of the channels on the long-term current, the time of 2 days that was always sufficient for the electrodes reach the maximum current, and the decoupling between current production and biofilm development, remain difficult to explain and open up exciting questions for future research on the mechanisms of electroactive biofilm formation.

Introduction

Microbial anodes are the cornerstone of most microbial electrochemical processes [1,2]. A huge number of studies have consequently aimed to improve their electrochemical performance. In this context, 3-dimensional porous electrodes have being increasingly used to offer the largest possible surface area for the development of the microbial electroactive biofilm [3]. Various types of porous electrodes have been implemented, mainly in the form of felts [4–6], foams [5,7,8], sponges [7,9–11], and multi-layered structures [12,13], made from a wide range of materials: carbon [14–18], including carbonaceous materials obtained by the pyrolysis of natural plants (pomelo peel, kenaf, corn stem, etc.) [19–21] and various metals [22–25].

A large range of pore sizes have been investigated, from some nanometres [26], through a few micrometres [27] and hundreds of micrometres [28] to several millimetres [11]. However, correlation between the bioelectrochemical performance of a 3-dimensional porous microbial anode and its pore size is not yet evident. A major obstacle that hinders the advance of knowledge in this area is the practical difficulty of designing experimental set-ups that allow access to the biofilm developing inside a porous structure. A recent study in this direction has described a stacked electrode configuration that allowed each layer to be independently imaged [12]. The purpose of the present study was to go ahead in this direction by designing a simple experimental set-up that would enable biofilm penetration inside a 3-dimensional structure to be approached. The main idea was to set a long (10 cm), flat electrode at the bottom of an insulating channel (Fig. 1) that could be disassembled at the end of the experiment in order to take images of the biofilm development along the electrode length. The width of the channel was chosen large enough (1 cm) not to impact the microbial colonization, so that the

* *Corresponding author.*
E-mail addresses: poehere.chog@ensiacet.fr (P. Chong), benjamin.erable@ensiacet.fr (B. Erable), alain.bergel@ensiacet.fr (A. Bergel).

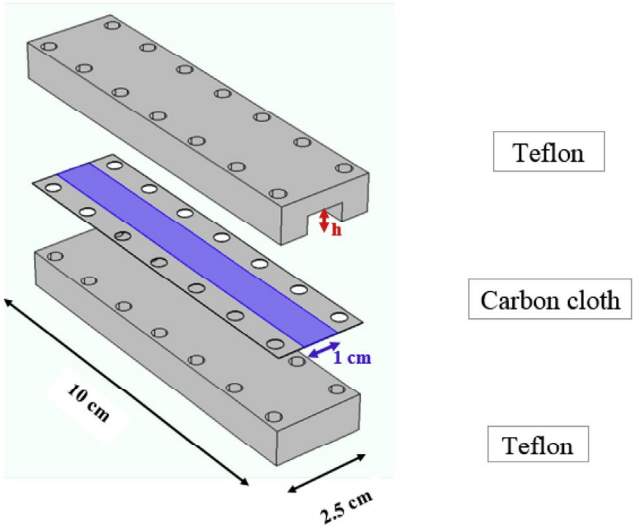

Fig. 1 – Schematic of the experimental channel device.

study could focus on the impact of the height of the channel as the sole parameter.

A quick glance at the literature helped in choosing characteristic sizes to work with. It is easy to accept that the narrowest pore sizes, smaller than cell sizes, cannot be accessed for biofilm development (although they may impact the performance of microbial anodes by other effects, like improving biofilm anchorage or the electron transfer rate [29]). Porous electrodes with pore sizes of a few micrometres been reported to be penetrated by microbial colonization, mostly when specific conditions were implemented with minimal synthetic media and pure cultures [6,27,30,31]. Nevertheless, larger pore sizes are required to avoid clogging by the biofilms that form in rich media. Clogging of the small pore sizes explains why open felts have been reported to produce current density similar to that of two-dimensional electrodes, for instance [32].

Considering that the thickness of mature electroactive biofilm can reach hundreds of micrometres [5,32,33], it can be speculated that pore sizes of a few millimetres may be the relevant choice to avoid pore clogging and allow the biofilm to upholster the largest possible surface area inside a porous structure. This kind of rule of thumb is supported by experimental results. The highest current densities reported so far with porous electrodes have generally been obtained with pore sizes of the order of millimetre [5,11,13] and multi-layered structures. Current density as high as 390 $A.m^{-2}$ has been reached with a multi-layered carbon anode with inter-layer distance of 1–3 mm [13]. Accordingly, channels characteristic sizes of 1 and 5 mm have been chosen in this study.

Materials and methods

Channel device fabrication

The channel device (Fig. 1) consisted of two rectangular parallelepiped parts (10 cm × 2.5 cm x 1 cm) made of Teflon. The upper part was machined with a channel along the whole length that was 1 cm wide and had two different heights, *h*: 1 mm (CH1) and 5 mm (CH5). A carbon cloth (Paxitech SAS France, France) was inserted between the upper and lower Teflon parts, thus forming an anode of 10 cm × 1.0 cm surface area applied against the bottom part. The anode was electrically connected with a platinum wire, whose part outside the carbon cloth was insulated with a heat-shrinkable sheath. The three pieces were assembled by means of 14 plastic screws uniformly distributed over the whole device. Insulating varnish (Electrofuge 200-ND, CRC Industries France SAS) was applied all around the outer section of the carbon cloth and dried overnight in a heat chamber at 40 °C.

Microbial anode formation

Primary bioanode formation

Primary bioanodes were first prepared to serve as the sole source of microbes for channel device and free electrodes experiments. They were formed using a garden compost leachate as the solution and inoculum. As described elsewhere [34], the leachate was obtained from a mixture of 1.5 L of garden compost and 2.25 L of tap water supplemented with 60 mM of KCl. This mixture was first stirred overnight at room temperature then filtered through a large-mesh cloth. The pH of the final compost leachate was 7.6 and its conductivity was 2.6 $S\ m^{-1}$.

The 3-electrode electrochemical reactors were composed of a carbon cloth (8 × 4 cm^2) as the working electrode (WE), a stainless steel grid as the counter electrode (CE) and a saturated calomel electrode (SCE, Radiometer, +0.242 V/SHE) as the reference electrode. The working electrode was electrically connected with a platinum wire, whose part outside the carbon cloth was insulated with a heat-shrinkable sheath. All potentials are expressed with respect to the SCE and current density values for these primary electrodes were calculated with respect to the whole anode surface area of 64 cm^2 (both 32 cm^2 faces of the electrode were exposed to the solution). Reactors were filled with 700 mL of garden compost leachate and deaerated by 15 min nitrogen bubbling. Primary bioanodes were formed by applying a constant potential (−0.20 V/SCE) with a multi-channel potentiostat (VMP BioLogic SA, France). Sodium acetate (20 mM), used as the substrate, was added every time the current density decreased to around 1 $A.m^{-2}$. Reactors were placed in a thermostatic bath to maintain the temperature at 40 °C. Primary bioanodes were considered mature, i.e. appropriate to be used as inoculum, when a stable current density of around 10 $A.m^{-2}$ was reached.

Formation of secondary bioanodes in the channel devices and on free electrodes

The channel devices were implemented in a batch reactor filled with 2.5 L of minimal synthetic medium composed of 50 mM bicarbonate buffer, 10 mL L^{-1} macronutrients, 1 mL L^{-1} micronutrients, 1 mL L^{-1} vitamins, 4.5 g L^{-1} KCl and 2.4 g L^{-1} $NaH_2PO_4 \cdot H_2O$ (see Supplementary Data Figure S.1). The mature primary bioanode used to inoculate the reactor was set at the centre. Three clean working electrodes were arranged circularly around the primary bioanode: two channel devices, one 1 mm high (CH1) and the other 5 mm high (CH5), and a free carbon cloth electrode used as the control. The free

electrode (a piece of commercial carbon cloth without any treatment) had the same dimensions as the electrode inside the channel devices, i.e. 10 cm × 1 cm, but both its sides were exposed to the solution, while only one side was exposed in the channel devices. Consequently, current densities were related to a surface area of 20 cm^2 for the free bioanodes and 10 cm^2 for the channel devices. The counter electrode was a circular platinum grid of 6 cm diameter, set above the primary bioanode.

The four electrodes (the primary bioanode used as the inoculum, the two channel devices and the free electrode) were individually addressed as WE polarized at −0.20 V/SCE with an N-stat device (Biologic SA, France) added to the multichannel potentiostat. The concentration of sodium acetate was measured periodically with an enzymatic kit (K-ACETAK, Megazymes) and maintained at 20 mM. Reactors were flushed with nitrogen for 20 min at the beginning and were maintained at 40 °C in a heat chamber. Experiments were performed at least in duplicate and up to 4 identical experiments were carried out for some conditions, as indicated in the Results section.

Microbial anode analysis

At the end of the experiment, the channel devices were disassembled and the bacterial colonization of the electrodes was assessed by epifluorescence microscopy and analysed by statistical analysis of the biofilm volume coverage ratios.

Epifluorescence microscopy. Biofilms were observed with a Carl Zeiss Axiomalger M2 microscope equipped for epifluorescence with an HBO 50 W ac mercury light source and the Zeiss 09 filter (excitor HP450-490, reflector FT 10, Barrier filter LP520). Images were acquired with a monochrome digital camera (evolution VF) every 0.5 μm along the Z-axis and the set of images was processed with the Axiovision® software. Electrodes were stained with acridine orange 0.01% (A6014 Sigma) for 10 min, then thoroughly rinsed in three different water baths before drying at room temperature. Acridine orange stains both the intracellular and extracellular nucleic acids and thus gives a fair representation of the global biofilm structure. To visualize the bacterial profile along the channel, images were taken every 1.5 cm along the electrode (eight different locations). For each location, four different spots were analysed and averaged, so 32 spots (8 locations x 4 spots) were analysed for each bioanode.

Biofilm volume coverage ratios. At each spot, a picture was built up to estimate the biofilm volume coverage ratio as described elsewhere [32,35]. For each picture, n images were taken along the z-axis, every 3.9 μm, forming a stack. For each image (i), the biofilm surface area ratio (Θ_i) was determined and then multiplied by the thickness of the layer (δ) and the image surface area A_{image} to calculate the local biofilm volume (V_i):

$$V_i = \theta_i \text{ x } \delta \text{ x } A_{image} \quad (1)$$

The final biofilm volume coverage ratio was calculated as:

$$\textit{Biofilm volume coverage ratio} = \sum_{i=1}^{n} V_i / V_T \quad (2)$$

where n varied between 50 and 80, depending on the biofilm thickness, and V_T was the total volume scanned by the n images:

$$V_T = n \text{ x } \delta \text{ x } A_{image} \quad (3)$$

Results

Choice of the experimental device

Inside a multi-layered structure or inside a pore of a monolithic electrode, mass transports occur in parallel to the length of the structure. The coupled transports and reactions inside such structures are usually modelled by making differential mass balances inside an elementary unit perpendicular to the main direction [36]. In an elementary unit, at stationary state, concentrations are assumed to be uniform and mass transport through the cross-sections balance the consumption or production by reaction on the electroactive surfaces (Fig. 2). This simplified approach allows establishing in an easy way a mono-dimensional transport-reaction equation:

$$d\phi i \; \textit{Cross} - \textit{section area} = \pm \frac{j}{n_i F} \; \textit{Differential reactive area} \quad (4)$$

where ϕ_i is molar flux of the species i, which can be described through the Nernst-Planck equation, j is the local current density, which may depend on concentrations of different species, n_i is the number of electron exchanged for the consumption/production of 1 mol of the species i, F is the Faraday constant; the sign - or + depends whether the i species is consumed or produced by the reaction, respectively.

For multi-layered electrodes, considering two electrode layers spaced of 2 h distance (Fig. 2) the *Cross-section area* is equal to 2 h l, were h is the half-distance of the electrode layers, and l is the width of the electrode layers, and the *Differential reactive area* is two-times $l\,dx$ because of the presence of two electrodes. The one-dimensional transport-reaction between two parallel, flat electrodes is thus:

$$d\phi i \; h = \pm \frac{j}{n_i F} \, dx \quad (5)$$

For the channel device elaborated in this study, the *Cross-section area* is equal to $h\,l$ and the *Differential reactive area* is $l\,dx$, so that the differential transport-reaction equation is also Eq. (5). Actually, the symmetry plane in the middle of two electrode layers is just replaced in the channel device by an insulating plane. Both kinds of interface correspond to Neumann boundary conditions, with the first derivative of the concentrations equal to zero. Consequently, the channel device with a height h gives a right model of what occurs inside a multi-layered structure with an inter-electrode distance of 2 h.

The relevancy of the channel device can enlarge by considering a cylindrical pore (Fig. 2). In this case the *Cross-section area* is equal to $\pi\, r^2$, were r is the pore radius, and the *Differential reactive area* is $2\pi\, r\, dx$, which leads to the differential transport-reaction equation:

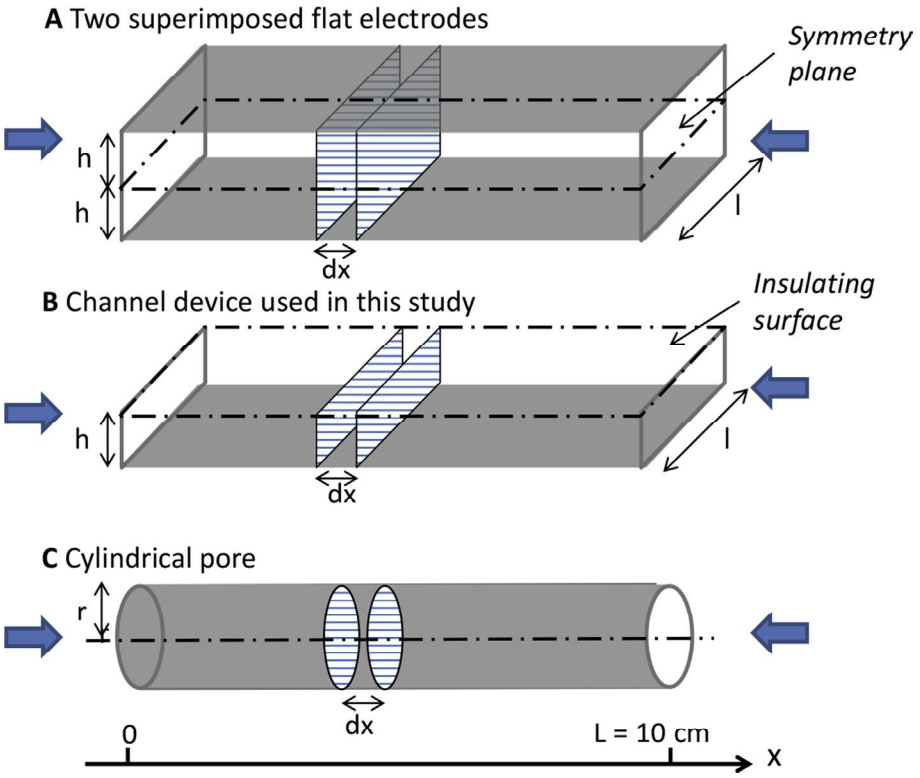

Fig. 2 – Schematic of one-directional transport for A) two adjacent layers of a multi-layered electrode B) the channel device used in this study, C) a cylindrical pore inside a monolithic electrode. The grey colour corresponds to the electrode surface; the hatched areas show the sections perpendicular to the x-axis, through which mass transports take place; the differential transport-reaction equation is established between two sections spaced of dx.

$$d\phi i\ \frac{r}{2} = \pm\frac{j}{n_i F}\ dx \qquad (6)$$

Comparing Eqs. (6) and (5) shows that a channel device with height h gives a relevant approach of a cylindrical pore with radius r equal to 2 h.

In conclusion, the channel devices with height h elaborated in this study give a relevant representation of the transport-reaction behaviour of multi-layered structured spaced by a distance 2 h and of cylindrical pores of radius 2 h.

Primary bioanode formation

Primary bioanodes were formed on carbon cloth electrodes polarized at −0.20 V/SCE in garden compost leachate with successive acetate additions (20 mM). The chronoamperometry curves of three bioanodes run in parallel gave fairly reproducible results (Fig. 3). After around 12 days of polarization, stable and mature electroactive biofilm had developed, which was consistent with previously reported studies [33, 34].

Secondary bioanodes in the channel devices and on the free electrodes

The primary bioanodes were used to form secondary bioanodes in a synthetic medium. Each reactor contained two electrodes in channel devices 1 and 5 mm high (CH1 and CH5 respectively) and a free electrode (control) of identical dimensions (1 cm × 10 cm). Experiments with 31 days of polarization were replicated 4 times in identical conditions. For the sake of clarity, the results of only one reactor are plotted in Fig. 4 the other results are provided in Supplementary Data (Fig. S2).

Free electrodes started to generate current after less than 20 h and reached current densities of around 15 A.m^{-2} during

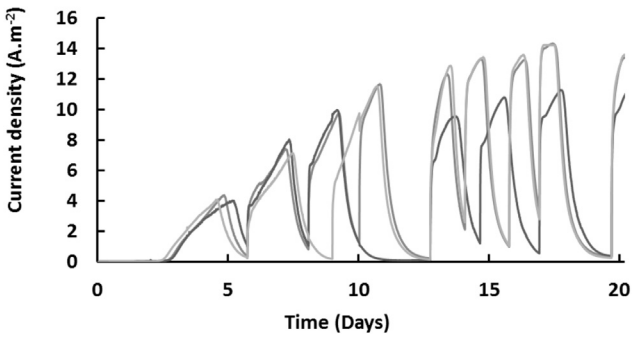

Fig. 3 – Chronoamperometry of primary bioanodes formed at −0.20 V/SCE with successive additions of 20 mM acetate to garden compost leachate at 40 °C. Acetate was added when current density fell to close to 0.

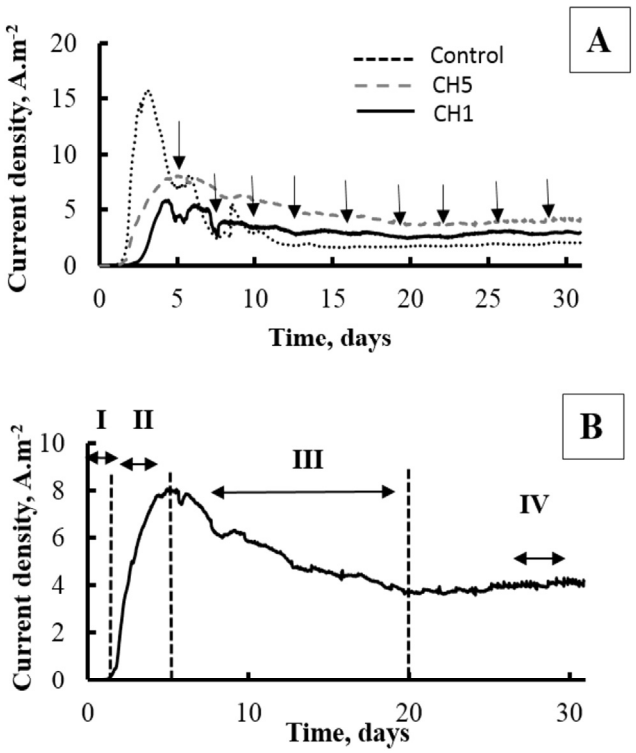

Fig. 4 – A) Chronoamperometry of secondary bioanodes formed at −0.20 V/SCE in synthetic medium at 40 °C during 31 days (arrows correspond to the acetate additions up to 20 mM) and B) Visualization of the 4 phases observed with a channel of 5 mm height.

the first 3 days. The CH1 and CH5 electrodes needed more time to start producing current, at least 1 and 2 days, respectively, and the maximum current densities remained 2.5 times lower than those of the free electrodes.

The initial behaviour of the free electrodes was similar for all replicates but their long-term performance showed more difference. For all free electrodes, the current decreased after a few days, but at different rates and, at the end of the 31 days of polarization, the free electrodes produced significantly different current densities - from near zero to 3 $A.m^{-2}$.

In comparison, the channel devices gave more stable results during the 31 days of experiment. Independently of the channel height, all the CH1 and CH5 chronoamperometry curves presented similar features, which can be described in four successive phases (Fig. 4B): I) an initial lag period, II) a rapid increase of the current density to a maximum value J_{max}, followed by III) a slow decrease, and ending by IV) a long-term stabilization of the current density at a value lower than J_{max}.

Effect of channel height on electrochemical performance

Four parameters were defined to characterize the formation phases of the secondary bioanodes: i) the start-up time, which corresponded to the duration of phase I and was defined as the time required for the initial current density reach 0.1 $A.m^{-2}$, ii) the maximum current density value J_{max}, iii) the duration of current increase (phase II), which was equal to the difference between the time at which J_{max} was reached and the start-up time, and iv) the value of the long-term current density. The mean value of each parameter is reported in Table 1. For the first three parameters, the mean value was based on values from ten experiments: quadruplicate of 31 days (Fig. 4A and Figure S.2) duplicate of 10 days (Fig. 5A and Figure S.3) and quadruplicate of 4 days (Fig. 5B and Figure S.4). The mean value of the fourth parameter (long-term current density) was obtained from the four experiments that lasted 31 days (Fig. 4A and Figure S2).

Some of the results reported in Table 1 could have been anticipated because of the geometric hindrance created on mass transport by the channel set-up:

- The free bioanodes started producing current at 0.8 days, while the bioanodes inside the channels started at 1.2 and 1.8 days for channel heights of 5 and 1 mm, respectively: decreasing the channel height from 5 to 1 mm increased the initial lag period by 50%.
- The bioanodes in the channel devices reached considerably lower maximum current density than the free bioanodes (5.4 ±1.5 vs. 13.1 ±2.9 $A.m^{-2}$).
- Decreasing the channel height from 5 to 1 mm decreased the long-term current density by 25%.

Some other results reported in Table 1 are more counter-intuitive:

- The channel height had no effect on the J_{max} value.
- Free bioanodes and bioanodes inside the different channels always showed an increasing phase (phase II) of two days; it always took two days for all bioanodes to reach the maximum current density, whatever the experimental set-up.
- The long-term current densities provided by CH1 and CH5 electrodes were respectively 30 and 70% higher than those of the free electrodes, suggesting that the channel configuration may favour current stability.

Effect of channel height on microbial colonization

Bioanodes were formed under identical conditions as previously described but polarization was stopped after 4 days (4 runs) and 10 days (2 runs). Four days of polarization approximately corresponded to the end of phase II, when the bioanodes reached maximum current density, and 10 days corresponded to the current decrease during the third phase. At the end of each experiment of 4, 10 or 31 days, the channel devices were dismantled and biofilm development was assessed by

Table 1 – Average values of the start-up time, J_{max}, duration of phase II (based on 10 experiments) and long-term current density (based on 4 experiments).

	Start-up time (days)	J max (A/m^2)	Duration Phase II (days)	Long term current (A/m^2)
Control	0.8 ± 0.1	13.1 ± 2.9	2 ± 0.6	1.7 ± 0.9
5 mm	1.2 ± 0.1	5.4 ± 1.5	2.2 ± 0.9	2.9 ± 1.0
1 mm	1.8 ± 0.5	5.4 ± 1.5	2.2 ± 1.1	2.2 ± 0.7

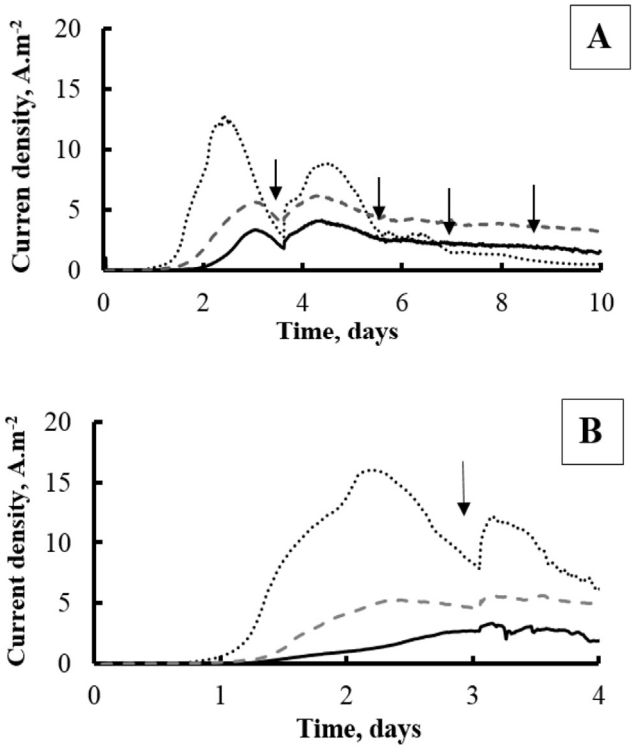

Fig. 5 – Chronoamperometry of secondary bioanodes formed at −0.20 V/SCE in synthetic medium at 40 °C during A) 10 and B) 4 days (arrows correspond to acetate additions).

epifluorescence microscopy. Pictures were taken along the 10 cm length of the electrodes at a regular distance of 1.5 cm. An example of the electrode colonization obtained after 31 days along the two channel heights is illustrated in Fig. 6.

Such image analysis was performed on duplicates of CH1 and CH5 bioanodes for each operation time (4, 10 and 31 days) to obtain the biofilm volume ratios along the electrode plotted in Fig. 7.

After 4 days, the full length of all bioanodes was colonized by bacteria. CH1 and CH5 provided biofilm volume ratios between 15 and 40%, with a slightly higher microbial density for CH1 bioanodes.

After 10 days, significant differences appeared depending on the channel height. The bioanodes in the 1 mm channels did not show significant evolution compared to their 4 day status and biofilm volume ratios remained less than 32% on most of the length of the bioanodes. In contrast, in the 5 mm channels, colonization had significantly increased. Biofilm volume ratios reached 55% at the extremities and around 30% at the centre.

After 31 days, the bioanodes in the 5 mm channels had kept the same general colonization profile as after 10 days, with only a global increase in the biofilm volume ratio of around 5%. In contrast, the bioanodes in the 1 mm channels showed significantly higher colonization than at day 10, particularly at the channel extremities, with biofilm volume ratios of up to 60%. The bioanodes in the 1 mm channels showed more pronounced colonization profiles, with a greater difference in biofilm coverage ratios between the centre and the extremities. The channels imposed some limiting constraint on colonization of the centre of the electrodes, and this constraint was stronger in the 1 mm channels.

Discussion

Initial internal colonization (phases I and II)

After 4 days, the full interior length of both CH1 and CH5 electrodes was totally colonized by bacteria (Fig. 7A). This confirmed observations already described in the literature [5,11,13,20] that millimetre pore sizes are fully appropriate for deep penetration of electroactive microorganisms. Here, it was shown that, after 4 days, the electrode colonization was almost uniform over the full electrode length, which means that the electroactive microorganisms could penetrate to significant depths, of several centimetres, inside channels at least 1 mm high. Accordingly, it might be concluded that a porous structure of a few millimetres in size could be implemented with several centimetres depth. Nevertheless, this conclusion must be qualified, because the maximum current densities, J_{max}, reached by the bioanodes inside the channels were significantly lower, around 2.5 times less, than those reached by the free bioanodes (Table 1).

The free bioanodes benefited from the continuous diffusion of acetate from the solution bulk, without any constraint. In contrast, the bioanodes confined in the channels probably consumed the 20 mM acetate contained in the volume of the channel first, and then had to wait for the diffusion of acetate through the small section area of the channel. It would be no surprise to find that this diffusion along narrow channels significantly limited the substrate supply. Consequently, during the initial phases of bioanode formation (phases I and II in Fig. 4), the free bioanodes and the bioanodes inside channels encountered very different situations in terms of substrate availability. The free bioanodes benefited from continuous, semi-infinite, linear diffusion with a very low ratio of electrode surface area to solution volume, equal to 8.10^{-3} cm^{-1} (20 cm^2 in 2.5 L). In contrast, for the bioanodes inside the channels, the initial phases I and II unfolded as if in a small vessel having the volume of the channel, with very high "electrode surface area/solution volume" ratios of 2 and 10 cm^{-1} for CH5 and CH1, respectively. It has been shown and theorized elsewhere [40] that a high ratio drastically limits the maximum current density that can be reached. Actually, in conditions of high electrode surface area/solution volume ratio, the fast depletion of the substrate precludes the full development of the electroactive biofilm. Here, the bioanodes formed inside the channels reached lower J_{max} than the free bioanodes because their initial formation occurred similarly to what could happen in a small closed vessel having the channel volume.

For a raw theoretical approach to this phenomenon, the time required for the 20 mM of acetate initially present in the volume of the two channel devices be totally consumed was calculated. The charge (Q, coulomb) provided by the initial 20 mM of acetate (C^0) contained in the channel device volume ($V_{CH} = \ell \times L \times h$) was:

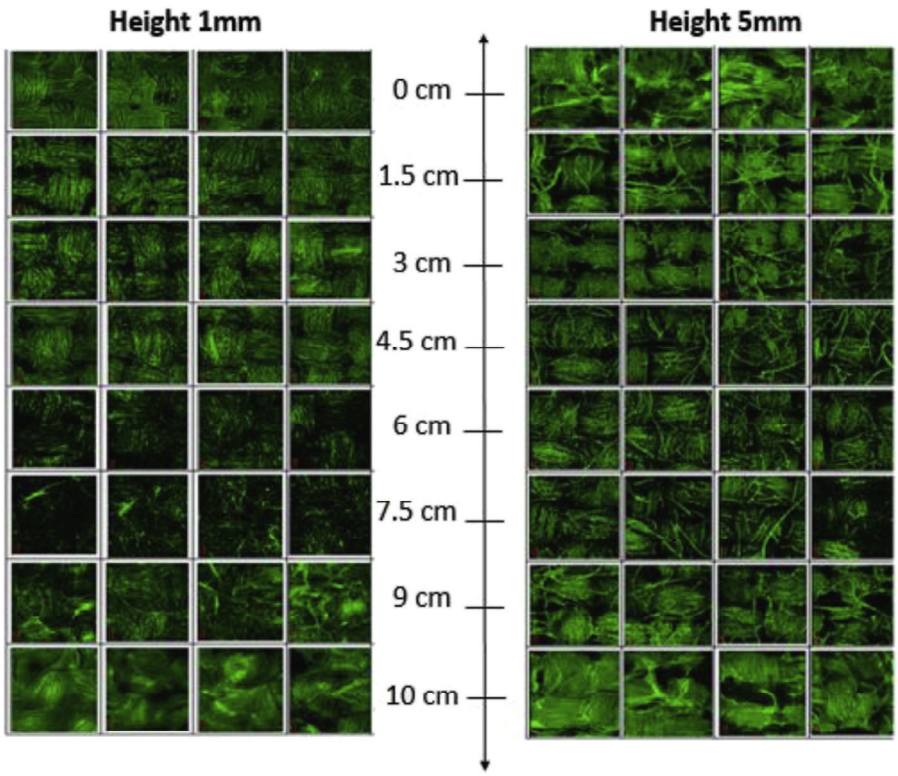

Fig. 6 – Biofilm profile inside channels of 1 and 5 mm height obtained by epifluorescence microscopy after 31 days of polarization; 4 spots were analysed for each of the 8 locations. (Colour). (For interpretation of the references to color in this figure legend, the reader is referred to the Web version of this article.)

$$Q = C^{\circ} n_e F V_{CH} \quad (7)$$

where ne = 8 is the number of moles of electrons consumed by the oxidation of 1 mol of acetate. Integrating the CA curves, from day 0 to different times, gave the time required for this charge be fully consumed by the electrochemical reaction, i.e. the time needed to consume the 20 mM acetate initially present inside the channel volume (Table 2). All the initial acetate was consumed after only 2 (CH5) and 2.3 (CH1) days of polarization. These times correspond to very early bioanode formation, at the beginning of phase II (Figs. 4 and 5).

Current then continued to increase for at least more than one day, showing that acetate transport from the bulk solution was an absolute requirement during the bioanode formation.

Theoretical approach to mass transport along the channels

Mass transport of the substrate to the electrode is essential and, in addition, it has been shown that mass transport can also severely impact the pH balance of bioanodes. Acetate oxidation led to the formation of protons:

$$CH_3COO^- + 4H_2O \rightarrow 2HCO_3^- + 9H^+ + 8e^- \quad (8)$$

From this equation, it appeared that 1 mol of acetate led to the formation of 9 mol of H^+ and 2 mol of HCO_3^-. Each mole of HCO_3^- can neutralize 1 mol of H^+ close to the electrode:

$$HCO_3^- + H^+ \rightarrow H_2CO_3 \quad (9)$$

This assumption is valid only at fairly low pH ($pK_a = 6.35$). Nevertheless, even if the carbonate produced by acetate oxidation consumed the maximum possible amount of protons, 7 mol of H^+ would still be produced for 1 mol of acetate consumed. The local accumulation of protons has been widely shown to adversely impact bacterial development and the biofilm electrocatalytic activity [41–44]. pH values of less than 6.7 have been shown to lower the electrochemical performance of bioanodes by killing the electroactive bacteria [45–47]. Dhar et al. measured the pH gradient inside enriched *Geobacter* spp biofilms (thickness around 130 μm) for concentrations of the phosphate buffer of 2.5, 50 and 100 mM. With phosphate concentrations of 2.5 and 50 mM, they found that local acidification ($pH \leq 6.6$) took place in the 40 μm thick inner layer of the bioanodes, which caused bacterial death. Current density was consequently decreased by 40% and 72%, for the phosphate concentrations of 50 mM and 2.5 mM, respectively, relative to that produced with 100 mM phosphate [33]. So, to mitigate local acidification near the bioanodes, buffering species must be transported from the bulk solution to the electrode.

In order to assess the impact of mass transport, a simple numerical approach was developed on the basis of the theoretical framework recently detailed elsewhere for microstructured electrode surfaces [29]. Transport of both the substrate (acetate) and the buffering species (HCO_3^-) inside the

Please cite this article in press as: Chong P, et al., Microbial anodes: What actually occurs inside pores?, International Journal of Hydrogen Energy (2018), https://doi.org/10.1016/j.ijhydene.2018.09.075

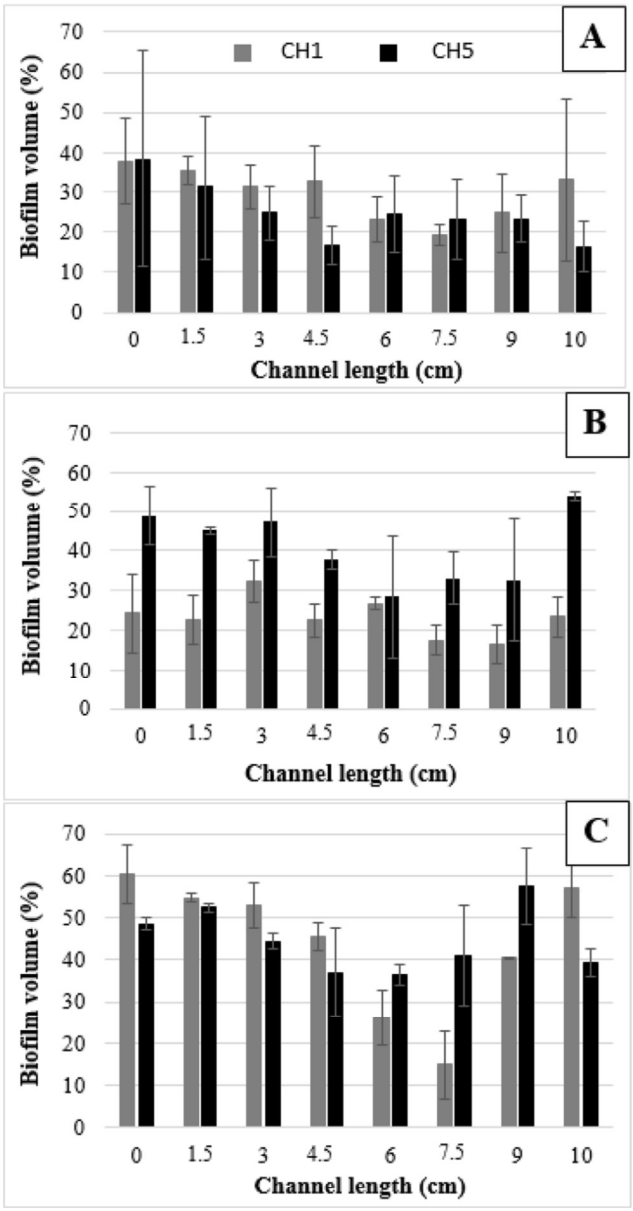

Fig. 7 – Average value of biofilm volume coverage ratios based on CH1 and CH5 electrodes (duplicates with 4 spots analysed for each at each location) after A) 4 days, B) 10 days and C) 31 days of polarization.

channels was modelled. In the present study, buffering was ensured by bicarbonate buffer at 50 mM, which means that the synthetic medium at pH 7.3 contained 45 mM of HCO_3^- ions able to neutralize the H^+ produced.

As demonstrated previously [29], in the vicinity of the anode surface, mass transport of acetate and HCO_3^- can be assumed to be mainly ensured by diffusion. Migration, playing a minor role, can be neglected. Inside the channels, diffusion is assumed to occur following the x axis across the section area of the channel and to be coupled with the consumption of acetate at the electrode surface (Fig. 2). The current is taken to be uniformly distributed along the electrode length. This assumption may be fairly valid during phases I and II, as the electrode colonization is not far from being uniform after 4 days (Fig. 7A). Then, the current probably diverges significantly from a uniform distribution. According to this approach, the differential mass balance done in an elementary unit of thickness *dx* (Eq. (5)), only involves the transport by diffusion, which leads to the continuity equation:

Table 2 – Parameter values used to determine the time needed to consume the initial 20 mM of acetate contained inside the channel volume; average values obtained from 6 experimental runs.

	C^0 (mol.m^{-3})	n_e	V_{CH} (m^3)	Q (C)	t (days)
1 mm	20	8	1×10^{-6}	15.4	2.3 ± 0.5
5 mm	20	8	5×10^{-6}	77.2	2.0 ± 0.2

$$D\frac{d^2C}{dx^2} = j_{anode}/(n\,F\,h) \tag{10}$$

where D (m^2.s^{-1}) is the diffusion coefficient of the species, C (mol.m^{-3}) the concentration, j_{anode} (A.m^{-2}) is the current density related to the anode surface area (10 cm^2), F is the Faraday constant (96 485 C mol^{-1}), *h* (m) is the channel height, and n_e is the number of electrons exchanged per mole of substrate consumed. According to the reaction (8), n = 8 for acetate and n = 8/7 for HCO_3^-, assuming that 2 protons are neutralized by the 2 molecules of HCO_3^- produced by the reaction, so that only 7 HCO_3^- molecules have to come from the bulk.

At the inlet of the channel (x = 0) the concentrations are assumed to be equal to the bulk concentration:

$$x = 0,\ C = C^{bulk} \tag{11}$$

Mass transport along the channels is assumed to have a plane of symmetry at the centre (Fig. 2), so that at x = L (L = 5 cm = half of the channel length) the first derivative of the concentration profiles is equal to zero:

$$X = L,\ \frac{dC}{dx} = 0 \tag{12}$$

With these two boundary conditions, solving Eq. (10) gives the concentration profiles along the electrode length:

$$C/C_0 = j_{anode}\,L^2/(n_e\,F\,h\,D\,C^{bulk})\ \ (x^2/(2L^2) - x/L) + 1 \tag{13}$$

where we have the modified Damköhler number Da_{mod} [48]:

$$Da_{mod} = (j_{anode}\,L)/(n_e\,F\,D\,C^{bulk}) \tag{14}$$

which characterizes the maximum consumption rate by the electrochemical reaction with respect to the maximum diffusion rate, and a geometric ratio:

$$\zeta = L/h \tag{15}$$

which corresponds to the ratio of one-half of the electrode surface area to the section area available for diffusion.

The products ξDa_{mod} (Table 3) were very much higher than 1 for both acetate and HCO_3^- and for both CH1 and CH2 configurations. This means that the consumption rates of acetate and HCO_3^- by the electrochemical reactions (8) and (9) were considerably faster than the maximal diffusion rates inside the channels. Obviously, the situation was worse for the

Table 3 – Parameter values used to model the diffusion of acetate and HCO_3^- inside the channel devices; the synthetic medium contained 50 mM of bicarbonate buffer at pH 7.3, which means 45 mM of HCO_3^- ions (pKa = 6.35); diffusion coefficients from Ref. [50].

	h (mm)	D ($m^2.s^{-1}$)	j_{anode} ($A.m^{-2}$)	n_e	C^{bulk} ($mol.m^{-3}$)	ζ	Da_{mod}	ζDa_{mod}
Acetate	1	$1.64\ 10^{-9}$	5.4	8	20	50	10.3	517
	5	$1.64\ 10^{-9}$	5.4	8	20	10	10.3	103
HCO_3^-	1	$1.18\ 10^{-9}$	5.4	8/7	45	50	46.2	2310
	5	$1.18\ 10^{-9}$	5.4	8/7	45	10	46.2	462

narrower channel (CH1). This simple theoretical approach confirms that mass transport of the substrate, and particularly of the buffering species, was strongly limited inside the channel electrodes.

Actually, such high values of the modified Damköhler number showed that the J_{max} value could not be sustained with a uniform distribution as assumed here for this simple approach. The value of J_{max} was certainly the result of a non-uniform distribution of J_{anode} along the electrode, with higher values at the extremities and lower ones in the central parts. Modelling this situation accurately would require taking the tertiary potential distribution [49] into account, which would be beyond the scope of the present study.

Following the initial colonization (phases II and III)

When the acetate initially contained in the channel volume had been completely consumed, i.e. towards the end of phase II (see section 4.1), biofilm development and electrochemical performance were limited by slow mass transfers (see section 4.2). Accordingly, the colonization profiles at days 10 and 31 showed a marked difference between the extremities of the channels and the centre. Biofilm volume ratios were always higher at the extremities and this difference was much more marked on the CH1 electrodes, in which mass transfer was the most constrained. For the same reason, colonization of the CH1 bioanodes was slower than that of the CH5 bioanodes; progress of the internal colonization took more time in the 1-mm-high channels, and the long-term current density was lower (Table 1). These observations are fully consistent with the mass transport limitation expressed by the Damköhler numbers.

Unsuspected observations and further research needs

In addition to the observations discussed in the three sections above, which were quite easy to explain, the original experimental set-up proposed here also revealed some unsuspected phenomena, opening up new avenues for further basic research on the mechanisms of electroactive biofilm formation.

It was intriguing to note that the start-up time (phase I), i.e. the time necessary for the current to start to be produced, was clearly impacted by the presence or absence of the channel and by the height of the channels (Table 1) while, in contrast, the time required for the current density to reach its maximum (duration of phase II) was not affected, and was equal to around 2 days in all cases. The early colonization of the electrode surface and the mechanisms by which bacteria approach the electrode and then start to organize an electroactive biofilm on the surface should be the subject of more intensive research, in particular because this early formation phase, during which the biofilm may be the most sensitive to external interventions, might be the most suitable period for driving the biofilm towards the highest possible electroactive efficiency. Here, the electroactive efficiency of the bioanodes inside the channels was fixed in two days. This observation strongly suggests that it will be essential to unravel the mechanisms at work during this short period in order to find levers to boost biofilm electroactivity. In this context, modelling the distribution of the Nernst potential along the electrode may be of interest as it has recently been demonstrated to impact the electroactivity of biofilms [35].

In the framework of unsuspected results, the decoupling between the evolution of the production of current and the progress of the colonization of the bioanode is noteworthy. The current reached its maximum at the end of phase II and then decreased (phase III) and stabilized (phase IV). In contrast, the biofilm volume continued to increase during phase III in the CH5 channels and even during phase IV in the CH1 channels (Fig. 7). Consequently, the current reached its maximum when bacterial colonization showed the lowest biofilm volume coverage ratios and, conversely, the lowest current density was produced at the end of the experiments when microbial colonization of both CH1 and CH5 bioanodes was found to be highest. These observations show the absence of direct correlation between the current density and the global microbial colonization inside a channel a few mm high, which contrasts with some previously reported results on open structures [29].

Several hypotheses can be suggested. The biofilm development might be related to thickening of the matrix, possibly with DNA release into the matrix, rather than multiplication of the cells. A proportion of the cells might also be dead, notably because of limiting mass transport, while others progress in colonizing the electrode surface. Biofilms may also continue to develop during phases III and IV with non-electroactive cells instead of anode-respiring bacteria. To support or reject these hypotheses, further work is currently in progress to characterize the status of the bioanodes by LIVE/DEAD staining after 4 days and 31 days of polarization and to compare the composition of the microbial communities by 16 S RNA sequencing.

Finally, in spite of the detrimental effects, the limited mass transport inside the channels revealed some possibly virtuous effects on the long-term stability here. The free bioanodes did not show excellent stability when maintained for several weeks, some showing drastic falls in current density while, in contrast, all the bioanodes inside channels

produced stable and more reproducible long-term current. Actually, our experience on the medium used here has shown that it was necessary to replace it periodically by fresh medium in order to maintain long-term current density [51]. This effect had so far been attributed to the possible depletion of some micro-nutrients or vitamins. Nevertheless, this hypothesis, which could explain part of the current decrease, cannot explain why the current was more stable inside channels.

The observation made here may suggest that the channel device could protect the biofilm by reducing the opportunities for electroactive bacteria to detach from the electrode surface. Obviously, the channel protected the electrode against all kinds of parasitic liquid movement, but the solution was not stirred and this protecting effect was probably limited. It can also be speculated that the limited mass transport inside the channels resulted in thinner biofilms, which were not at a sufficiently advanced state of development to trigger dispersal mechanisms. When the population density of biofilms reaches a threshold level, internal signals can be produced that induce biofilm dispersion [52]. The signalling molecules are produced in the deepest layers [53] or are linked to quorum sensing [54]. Here, limited mass transports in the channels may keep the biofilm in an under-developed state, below the threshold where dispersal occurs, while, in contrast, the dispersal phenomena are fully operational in free bioanodes. Further basic research is needed to confirm this hypothesis, which may open up a new way to design bioanode structures and could enhance the stability of current density by limiting the development state of the biofilm.

Conclusion

The mechanisms of electroactive biofilm settlement inside pores are far from being fully deciphered and designing optimal microbial porous anodes is a fascinating challenge for electrochemical engineers. In this context, an innovative analytical set-up has been presented here. Some of the experimental observations it has brought can be explained by the analysis of mass transports along the channels, while others, more difficult to anticipate, open up intriguing research questioning. In particular, the clear decoupling between the production of current and biofilm development should be an exciting and promising topic to investigate in further research works. Practically, it can be kept in mind that a porosity size of a few millimetres allows electrode colonization on several centimetres of penetration depth and enhances the stability of current density. Nevertheless, it clearly impacts the evolution of the biofilm and limits the maximum current density that can be reached.

Acknowledgements

This work was supported by the French state, managed by the Agence Nationale de la Recherche (ANR), within the framework of the Bioelec project (ANR-13-BIME-006) and the "Koropokkuru" project (ANR-14-CE05-0004).

Appendix A. Supplementary data

Supplementary data to this article can be found online at https://doi.org/10.1016/j.ijhydene.2018.09.075.

REFERENCES

[1] Wang H, Ren ZJ. A comprehensive review of microbial electrochemical systems as a platform technology. Biotechnol Adv 2013;31:1796–807. https://doi.org/10.1016/j.biotechadv.2013.10.001.

[2] Santoro C, Arbizzani C, Erable B, Ieropoulos I. Microbial fuel cells: from fundamentals to applications. A review. J Power Sources 2017;356:225–44. https://doi.org/10.1016/j.jpowsour.2017.03.109.

[3] Xie X, Criddle C, Cui Y. Design and fabrication of bioelectrodes for microbial bioelectrochemical systems. Energy Environ Sci 2015;8:3418–41. https://doi.org/10.1039/C5EE01862E.

[4] Lepage G, Albernaz FO, Perrier G, Merlin G. Characterization of a microbial fuel cell with reticulated carbon foam electrodes. Bioresour Technol 2012;124:199–207. https://doi.org/10.1016/j.biortech.2012.07.067.

[5] Ketep SF, Bergel A, Calmet A, Erable B. Stainless steel foam increases the current produced by microbial bioanodes in bioelectrochemical systems. Energy Environ Sci 2014;7:1633–7. https://doi.org/10.1039/c3ee44114h.

[6] Yang Y, Liu T, Zhu X, Zhang F, Ye D, Liao Q, et al. Boosting power density of microbial fuel cells with 3D nitrogen-doped graphene aerogel electrode. Adv Sci 2016;3. https://doi.org/10.1002/advs.201600097.

[7] Liu X, Du X, Wang X, Li N, Xu P, Ding Y. Improved microbial fuel cell performance by encapsulating microbial cells with a nickel-coated sponge. Biosens Bioelectron 2013;41:848–51. https://doi.org/10.1016/j.bios.2012.08.014.

[8] Wang H, Wang G, Ling Y, Qian F, Song Y, Lu X, et al. High power density microbial fuel cell with flexible 3D graphene-nickel foam as anode. Nanoscale 2013;5:10283–90. https://doi.org/10.1039/c3nr03487a.

[9] Xie X, Yu G, Liu N, Bao Z, Criddle CS, Cui Y. Graphene–sponges as high-performance low-cost anodes for microbial fuel cells. Energy Environ Sci 2012;5:6862–6. https://doi.org/10.1039/C2EE03583A.

[10] Xie X, Meng Y, Yi C. Cabone nanotube-coated macroporous sponge for microbial fuel cell electrodes. 2012. p. 5265–70. https://doi.org/10.1039/C1EE02122B.

[11] Liu M, Zhou M, Yang H, Zhao Y, Hu Y. A cost-effective polyurethane based activated carbon sponge anode for high-performance microbial fuel cells. RSC Adv 2015;5:84269–75. https://doi.org/10.1039/C5RA14644E.

[12] Artyushkova K, Roizman D, Santoro C, Doyle LE, Fatima Mohidin A, Atanassov P, et al. Anodic biofilms as the interphase for electroactive bacterial growth on carbon veil. Biointerphases 2016;11:031013. https://doi.org/10.1116/1.4962264.

[13] Chen S, He G, Liu Q, Harnisch F, Zhou Y, Chen Y, et al. Layered corrugated electrode macrostructures boost microbial bioelectrocatalysis. Energy Environ Sci 2012;5:9769–72. https://doi.org/10.1039/C2EE23344D.

[14] Chen S, Hou H, Harnisch F, Patil SA, Carmona-Martinez AA, Agarwal S, et al. Electrospun and solution blown three-dimensional carbon fiber nonwovens for application as electrodes in microbial fuel cells. Energy Environ Sci 2011;4:1417–21. https://doi.org/10.1039/C0EE00446D.

[15] Chen S, He G, Carmona-Martinez AA, Agarwal S, Greiner A, Hou H, et al. Electrospun carbon fiber mat with layered architecture for anode in microbial fuel cells. Electrochem Commun 2011;13:1026–9. https://doi.org/10.1016/j.elecom.2011.06.009.
[16] Wang Y-Q, Huang H-X, Li B, Li W-S. Novelly developed three-dimensional carbon scaffold anodes from polyacrylonitrile for microbial fuel cells. J Mater Chem A 2015;3:5110–8. https://doi.org/10.1039/C4TA06007E.
[17] Huang L, Li X, Ren Y, Wang X. A monolithic three-dimensional macroporous graphene anode with low cost for high performance microbial fuel cells. RSC Adv 2016;6:21001–10. https://doi.org/10.1039/C5RA24718G.
[18] Ren H, Tian H, Gardner CL, Ren T-L, Chae J. A miniaturized microbial fuel cell with three-dimensional graphene macroporous scaffold anode demonstrating a record power density of over 10 000 W m(-3). Nanoscale 2016;8:3539–47. https://doi.org/10.1039/c5nr07267k.
[19] Karthikeyan R, Wang B, Xuan J, Wong JWC, Lee PKH, Leung MKH. Interfacial electron transfer and bioelectrocatalysis of carbonized plant material as effective anode of microbial fuel cell. Electrochim Acta 2015;157:314–23. https://doi.org/10.1016/j.electacta.2015.01.029.
[20] Yuan Y, Zhou S, Liu Y, Tang J. Nanostructured macroporous bioanode based on polyaniline-modified natural loofah sponge for high-performance microbial fuel cells. Environ Sci Technol 2013;47:14525–32. https://doi.org/10.1021/es404163g.
[21] Chen S, Liu Q, He G, Zhou Y, Hanif M, Peng X, et al. Reticulated carbon foam derived from a sponge-like natural product as a high-performance anode in microbial fuel cells. J Mater Chem 2012;22:18609–13. https://doi.org/10.1039/c2jm33733a.
[22] Hou J, Liu Z, Yang S, Zhou Y. Three-dimensional macroporous anodes based on stainless steel fiber felt for high-performance microbial fuel cells. J Power Sources 2014;258:204–9. https://doi.org/10.1016/j.jpowsour.2014.02.035.
[23] Massazza D, Parra R, Busalmen JP, Romeo HE. New ceramic electrodes allow reaching the target current density in bioelectrochemical systems. Energy Environ Sci 2015;8:2707–12. https://doi.org/10.1039/C5EE01498K.
[24] Baudler A, Schmidt I, Langner M, Greiner A, Schroeder U. Does it have to be carbon? Metal anodes in microbial fuel cells and related bioelectrochemical systems. Energy Environ Sci 2015;8:2048–55. https://doi.org/10.1039/c5ee00866b.
[25] Liu M, Zhou M, Yang H, Ren G, Zhao Y. Titanium dioxide nanoparticles modified three dimensional ordered macroporous carbon for improved energy output in microbial fuel cells. Electrochim Acta 2016;190:463–70. https://doi.org/10.1016/j.electacta.2015.12.131.
[26] Qiao Y, Bao S-J, Li CM, Cui X-Q, Lu Z-S, Guo J. Nanostructured polyaniline/titanium dioxide composite anode for microbial fuel cells. ACS Nano 2008;2:113–9. https://doi.org/10.1021/nn700102s.
[27] Zhao S, Li Y, Yin H, Liu Z, Luan E, Zhao F, et al. Three-dimensional graphene/Pt nanoparticle composites as freestanding anode for enhancing performance of microbial fuel cells. Sci Adv 2015;1:e1500372. https://doi.org/10.1126/sciadv.1500372.
[28] Chen W, Huang Y-X, Li D-B, Yu H-Q, Yan L. Preparation of a macroporous flexible three dimensional graphene sponge using an ice-template as the anode material for microbial fuel cells. RSC Adv 2014;4:21619–24. https://doi.org/10.1039/C4RA00914B.
[29] Champigneux P, Renault-Sentenac C, Bourrier D, Rossi C, Delia M-L, Bergel A. Effect of surface nano/micro-structuring on the early formation of microbial anodes with Geobacter sulfurreducens: experimental and theoretical approaches. Bioelectrochem n.d. doi:10.1016/j.bioelechem.2018.02.005.
[30] Lin X, Nishio K, Konno T, Ishihara K. The effect of the encapsulation of bacteria in redox phospholipid polymer hydrogels on electron transfer efficiency in living cell-based devices. Biomater 2012;33:8221–7. https://doi.org/10.1016/j.biomaterials.2012.08.035.
[31] Jiang H, Halverson LJ, Dong L. A miniature microbial fuel cell with conducting nanofibers-based 3D porous biofilm. J Micromech Microeng 2015;25:125017. https://doi.org/10.1088/0960-1317/25/12/125017.
[32] Blanchet E, Erable B, De Solan M-L, Bergel A. Two-dimensional carbon cloth and three-dimensional carbon felt perform similarly to form bioanode fed with food waste. Electrochem Commun 2016;66:38–41. https://doi.org/10.1016/j.elecom.2016.02.017.
[33] Dhar BR, Sim J, Ryu H, Ren H, Santo Domingo JW, Chae J, et al. Microbial activity influences electrical conductivity of biofilm anode. Water Res 2017;127:230–8. https://doi.org/10.1016/j.watres.2017.10.028.
[34] Cercado B, Byrne N, Bertrand M, Pocaznoi D, Rimboud M, Achouak W, et al. Garden compost inoculum leads to microbial bioanodes with potential-independent characteristics. Bioresour Technol 2013;134:276–84. https://doi.org/10.1016/j.biortech.2013.01.123.
[35] Oliot M, Chong P, Erable B, Bergel A. Influence of the electrode size on microbial anode performance. Chem Eng J 2017;327:218–27. https://doi.org/10.1016/j.cej.2017.06.044.
[36] Green DW, Perry RH. Perry's chemical engineers' handbook. 8th ed. New York, NY: McGraw-Hill Professional; 2007.
[40] Rimboud M, Pocaznoi D, Erable B, Bergel A. Electroanalysis of microbial anodes for bioelectrochemical systems: basics, progress and perspectives. Phys Chem Chem Phys 2014;16:16349–66. https://doi.org/10.1039/C4CP01698J.
[41] Torres CI, Kato Marcus A, Rittmann BE. Proton transport inside the biofilm limits electrical current generation by anode-respiring bacteria. Biotechnol Bioeng 2008;100:872–81. https://doi.org/10.1002/bit.21821.
[42] Gil G-C, Chang I-S, Kim B-H, Kim M, Jang J-K, Park HS, et al. Operational parameters affecting the performance of a mediator-less microbial fuel cell. Biosens Bioelectron 2003;18:327–34.
[43] Popat SC, Torres CI. Critical transport rates that limit the performance of microbial electrochemistry technologies. Bioresour Technol 2016;215:265–73. https://doi.org/10.1016/j.biortech.2016.04.136.
[44] Harnisch F, Schröder U. Selectivity versus mobility: separation of anode and cathode in microbial bioelectrochemical systems. Chem Sus Chem 2009;2:921–6. https://doi.org/10.1002/cssc.200900111.
[45] Patil SA, Harnisch F, Koch C, Hübschmann T, Fetzer I, Carmona-Martínez AA, et al. Electroactive mixed culture derived biofilms in microbial bioelectrochemical systems: the role of pH on biofilm formation, performance and composition. Bioresour Technol 2011;102:9683–90. https://doi.org/10.1016/j.biortech.2011.07.087.
[46] Kim M-S, Lee Y. Optimization of culture conditions and electricity generation using Geobacter sulfurreducens in a dual-chambered microbial fuel-cell. Int J Hydrogen Energy 2010;35:13028–34. https://doi.org/10.1016/j.ijhydene.2010.04.061.
[47] Franks AE, Nevin KP, Jia H, Izallalen M, Woodard TL, Lovley DR. Novel strategy for three-dimensional real-time imaging of microbial fuel cell communities: monitoring the inhibitory effects of proton accumulation within the anode biofilm. Energy Environ Sci 2008;2:113–9. https://doi.org/10.1039/B816445B.

[48] Scott K, Sun Y-P. Approximate analytical solutions for models of three-dimensional electrodes by adomian's decomposition method. Mod. Asp. electrochem. New York, NY: Springer; 2007. p. 221–304. https://doi.org/10.1007/978-0-387-46108-3_4.
[49] Lacroix R, Silva SD, Gaig MV, Rousseau R, Délia M-L, Bergel A. Modelling potential/current distribution in microbial electrochemical systems shows how the optimal bioanode architecture depends on electrolyte conductivity. Phys Chem Chem Phys 2014;16:22892–902. https://doi.org/10.1039/C4CP02177K.
[50] Wilke CR, Chang P. Correlation of diffusion coefficients in dilute solutions. AIChE J 1955;1:264–70. https://doi.org/10.1002/aic.690010222.
[51] Oliot M, Etcheverry L, Mosdale A, Basseguy R, Délia M-L, Bergel A. Separator electrode assembly (SEA) with 3-dimensional bioanode and removable air-cathode boosts microbial fuel cell performance. J Power Sources 2017;356:389–99. https://doi.org/10.1016/j.jpowsour.2017.03.016.
[52] Boles BR, Horswill AR. Agr-mediated dispersal of Staphylococcus aureus biofilms. PLoS Pathog 2008;4:e1000052. https://doi.org/10.1371/journal.ppat.1000052.
[53] Rendueles O, Ghigo J-M. Multi-species biofilms: how to avoid unfriendly neighbors. FEMS Microbiol Rev 2012;36:972–89. https://doi.org/10.1111/j.1574-6976.2012.00328.x.
[54] Solano C, Echeverz M, Lasa I. Biofilm dispersion and quorum sensing. Curr Opin Microbiol 2014;18:96–104. https://doi.org/10.1016/j.mib.2014.02.008.